A Thicknessless Method for the Low-Loss Dielectric Characterization from Free-Space Scattering Measurements

Sung Kim, *Member, IEEE*, David Novotny, Joshua Gordon, *Member, IEEE*, and Jeffrey Guerrieri, *Member, IEEE*

***Abstract*—A free-space measurement method is presented for the characterization of low-loss dielectric materials at millimeter-wave (MMW) frequencies that does not require any assumption of *a priori* knowledge of the sample thickness. The present method first employs only maximal and minimal envelopes of measured transmission scattering parameters as to determine the real part ε_r' of the permittivity of the test material. Subsequently, the thickness of the sample is estimated from ε_r' and frequencies for maximal and minimal peaks of the transmission scattering parameter, and then calculation of the imaginary part ε_r" of the permittivity easily follows. Our method is examined by measuring two cross-linked polystyrene (XLPS) samples, one polytetrafluoroethylene (PTFE) sample, and one polymethylpentene (PMP) sample in the frequency range of 220-325 GHz at incident angles of 0, 10, 20, and 30 degrees. Moreover, an explicit uncertainty analysis for the permittivity is derived, and uncertainties of the extracted permittivity in real and imaginary parts are reported.**

***Index Terms*—Bistatic scattering, dielectric permittivity, free-space measurement method, fringing spectra, low loss materials, millimeter-wave (MMW) measurements, scattering parameter envelopes.**

I. Introduction

Low-loss dielectric materials have been widely employed to manufacture substrates, resonators, filters, lenses, etc., to integrate in a variety of communications systems, measurement equipment, and sensors constructed in the electronics industry [1, 2]. Electromagnetic characterizations of low-loss dielectric materials have been in high demand and have been greatly improved in numerous research activities [3, 4].

The methods for characterizing materials are conventionally classified into several different types, depending upon measurement conditions—whether we measure a broad or narrow band, whether we deal with a low-loss or highly lossy material, and whether we characterize dielectric and/or magnetic properties, etc. [3, 4] The free-space measurement method that uses the transmission and/or reflection scattering parameters measured for a test material inserted between transmit and receive antennas has become widespread as one of the methods for low-loss dielectric characterizations at broad-band millimeter-wave (MMW) frequencies [5-12]. The free-space measurement method has also suited a nondestructive evaluation (NDE) technique because there is no requirement for extreme care of machining of a test sample and there is no need for the contact with a sample [4].

An advent of the conventional free-space measurement method for dielectric-material characterizations dates a number of decades back to the work at the MIT Radiation Laboratory [5]. Thereafter, Breeden [6] demonstrated a low-loss dielectric measurement based on the method [5] at a MMW frequency and provided a thorough error analysis for the measurement. Alternatively, Campbell [7] derived a method for characterizing the dielectric permittivity simply from the Brewster's angle and the magnitude of the transmission coefficient measured for a test material, developed the measurement system, and demonstrated dielectric measurements with such a system.

In last several decades, the emergence of vector network analyzers (VNAs) has promoted dissemination of free-space measurements from research laboratories to industrial facilities. Varadan *et al.* developed the handily-implemented free-space method for dielectric characterizations that use only reflection parameter measurements by a VNA at microwave frequencies [8], and demonstrated the free-space method that employs only transmission parameters for dielectric measurements at high temperature [9]. Varadan *et al.* [10] further extended the method to simultaneously measure both of the permittivity and permeability from transmission and reflection parameters at microwave frequencies. Friedsam and Biebl [11] constructed the free-space measurement system that enables dielectric characterizations with a normal and/or oblique-incidence illumination at 75-94 GHz. In recent years, the free-space measurement for dielectric materials has been demonstrated with the VNA up to 300 GHz [12]. All of the conventional free-space measurement methods that have been developed assume that a plane-wave is illuminated upon a sample and the sample thickness is precisely known.

In contrast to the conventional free-space measurement methods for microwave/MMW frequencies, the permittivity of dielectric thin films on substrates has been widely determined from maximal and/or minimal envelopes of measured

Manuscript received MM DD, 2016.

The authors are with the Radio Frequency Technology Division, Communications Technology Laboratory, National Institute of Standards and Technology, Boulder, CO 80305 USA (sung.x.kim@nist.gov).

transmission/reflection spectra rather than from scattering parameters themselves at wavelengths of visible light [13-17]. Many of these methods extracted the permittivity from maximal and/or minimal envelopes only of reflection spectra without any knowledge of the film thickness because test material films were preliminarily deposited on substrates. In many of these studies, the envelope method has been demonstrated by use of only normal-incidence illuminations. We find very worth-reading discussions on theoretical backgrounds, very detailed formulations for the envelope method, as well as judicious investigations of applicability of the envelope method in Swanepoel's [18] and Martínez-Antón's [19] articles. Moreover, we find another similar method [20] proposed to extract the refractive index of a dielectric film in the far-infrared range but with the prerequisite knowledge of the film thickness.

At the National Institute of Standards and Technology (NIST), we have formerly developed a bidirectional scattering measurement system in the free-space setting based on a VNA that allows us to measure transmission and reflection scattering parameters at MMW frequencies [21]. In [21], we have validated the system's capability of measurements for bidirectional reflectance distribution functions (BRDFs) for various material samples of small size that requires measuring the reflection scattering parameter with the receive antenna angle being varied and with the sample angle being held constant. At present, we are able to conduct dielectric characterizations with the free-space measurement method at MMW frequencies, and all transmission and reflection measurements can be performed with the bidirectional scattering measurement system constructed at NIST.

In this paper, the free-space measurement method for extracting the complex permittivity of a low-loss dielectric material is developed without any assumption of *a priori* knowledge of the sample thickness. All of the aforementioned conventional free-space methods for microwave and MMW measurements need to know the sample thickness, whereas the present method can determine the real part of the permittivity of a low-loss dielectric material immediately only from maximal and minimal envelopes of the transmission scattering parameter measured for a test sample. Consecutively, the sample thickness is calculated from the real part of the permittivity and frequencies for the maximal and minimum peaks of the transmission scattering parameter. The imaginary part of the permittivity is then found from the real part of the permittivity and the sample thickness. We also derive explicit expressions for uncertainties for the real and imaginary parts of the permittivity obtained with the present method.

Our method is examined by measuring three different low-loss materials, cross-linked polystyrene (XLPS), polytetrafluoroethylene (PTFE), and polymethylpentene (PMP), from 220-325 GHz at 0, 10, 20, and 30 degrees. Experimental results from the present method are discussed, and uncertainties in real and imaginary parts of the permittivity of these materials are evaluated.

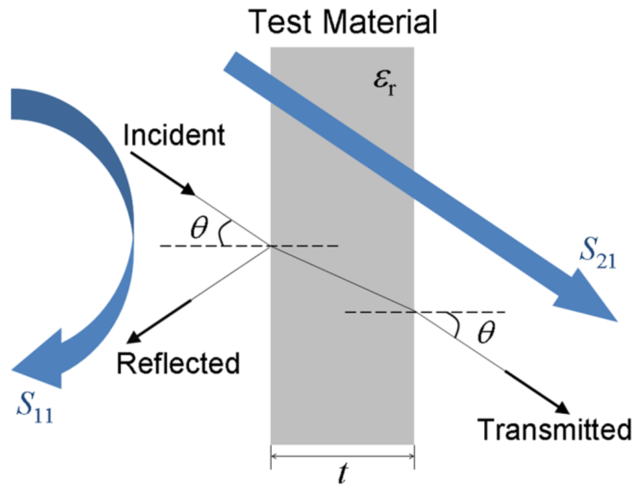

Fig. 1. Schematic of the transmission and reflection scattering parameters measured for a test material with the bidirectional scattering measurement system in the free space setting.

II. Formulation

A. Equations for Extracting ε_r'

Consider the transmission and reflection scattering parameters measured with the bidirectional scattering measurement system in the free-space setting as shown in Fig. 1. Taking into account multiple reflections occurring within the material immersed in air, and assuming that properties of the test material are linear and homogeneous (not necessarily isotropic), the transmission and reflection scattering parameters measured for the test material sample are respectively written as

$$S_{21} = \frac{\left(1-\Gamma^2\right)\exp(-j\beta)}{1-\Gamma^2\exp(-j2\beta)}, \quad (1)$$

$$S_{11} = \frac{\Gamma\left[1-\exp(-j2\beta)\right]}{1-\Gamma^2\exp(-j2\beta)}, \quad (2)$$

where $j=\sqrt{-1}$, Γ is the reflection coefficient of the interface, which we let define as $\Gamma = \Gamma^{\mathrm{r}} + j\Gamma^{\mathrm{i}}$ here, and β is given by

$$\beta = \beta^{\mathrm{r}} + j\beta^{\mathrm{i}} = \frac{2\pi t}{\lambda_0}\sqrt{\varepsilon_{\mathrm{r}} - \sin^2\theta}, \quad (3)$$

where t is the sample thickness, λ_0 is the wavelength in the air, ε_{r} is the complex relative permittivity of the test material, and θ is the incident angle.

We begin our formulation by deriving the expression for the maximal and minimal envelopes of $|S_{21}|$. From (1), we get the amplitude of S_{21}, that is

$$|S_{21}|^2 = S_{21}S_{21}^* = \frac{\left(1-2\,\mathrm{Re}\left[\Gamma^2\right]+|\Gamma|^4\right)\exp\left(2\beta^{\mathrm{i}}\right)}{1+|\Gamma|^4\exp\left(4\beta^{\mathrm{i}}\right)-2\exp\left(2\beta^{\mathrm{i}}\right)\mathrm{Re}\left[\Gamma^2\exp\left(-j2\beta^{\mathrm{r}}\right)\right]}. \quad (4)$$

The symbol $*$ in the above equation denotes the complex conjugate. From (4), given an assumption that we measure a low-loss dielectric material and that $\Gamma^{\mathrm{r}} \gg \Gamma^{\mathrm{i}}$ allowing for the approximation $\mathrm{Re}\left[\Gamma^2\right] \cong |\Gamma|^2 = \Gamma^2$, we achieve

$$|S_{21}|^2 = \frac{\left(1-|\Gamma|^2\right)^2\exp\left(2\beta^{\mathrm{i}}\right)}{1+|\Gamma|^4\exp\left(4\beta^{\mathrm{i}}\right)-2|\Gamma|^2\exp\left(2\beta^{\mathrm{i}}\right)\cos\left(2\beta^{\mathrm{r}}\right)}. \quad (5)$$

In (5), we see that $|S_{21}|^2$ attains its maximal and minimal value respectively when $\beta^{\mathrm{r}} = m\pi$ and $\beta^{\mathrm{r}} = (2m+1)\pi/2$ where m is an integer ($m = 0,1,2,\ldots$). Therefore, we obtain equations for the envelopes, $T_{\max}$ and $T_{\min}$, of maximal and minimal $|S_{21}|^2$ represented by

$$T_{\max} = \frac{\left(1-|\Gamma|^2\right)^2\exp\left(2\beta^{\mathrm{i}}\right)}{\left[1-|\Gamma|^2\exp\left(2\beta^{\mathrm{i}}\right)\right]^2}, \quad (6)$$

$$T_{\min} = \frac{\left(1-|\Gamma|^2\right)^2\exp\left(2\beta^{\mathrm{i}}\right)}{\left[1+|\Gamma|^2\exp\left(2\beta^{\mathrm{i}}\right)\right]^2}. \quad (7)$$

Note that (5), (6), and (7) are a function of the frequency f or the incident angle θ. Figs. 2(a) and (b) show illustrative plots of $|S_{21}|^2$, $T_{\max}$, and $T_{\min}$ as a function of f and θ. From (6) and (7), we further obtain

$$\exp\left(\beta^{\mathrm{i}}\right) = \frac{\sqrt{T_{\max}T_{\min}} \pm \sqrt{T_{\max}T_{\min}+T_{\max}-T_{\min}}}{\sqrt{T_{\max}}+\sqrt{T_{\min}}}, \quad (8)$$

$$|\Gamma|^2\exp\left(2\beta^{\mathrm{i}}\right) = \frac{\sqrt{T_{\max}}-\sqrt{T_{\min}}}{\sqrt{T_{\max}}+\sqrt{T_{\min}}}. \quad (9)$$

Along with the maximal and minimal envelopes, $T_{\max}$ and $T_{\min}$, of measured $|S_{21}|^2$, (8) and (9) allow us to calculate the reflection coefficient Γ without any *a priori* knowledge of the sample thickness t. The sign in (8) should be chosen so that $0 < \exp\left(\beta^{\mathrm{i}}\right) \le 1$. In finding proper Γ from (9) with (8), the reflection coefficient Γ is mostly $\Gamma \le 0$ at small incident angles when measuring a dielectric material.

In the same manner as was worked out for S_{21}, we get the amplitude of S_{11} that results in

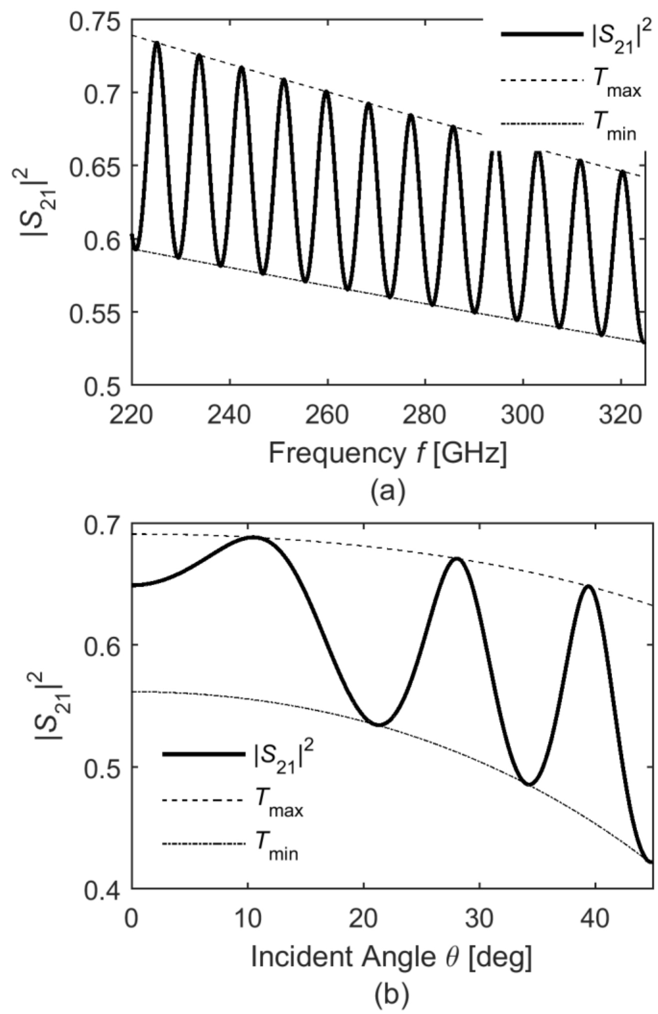

Fig. 2. $|S_{21}|^2$, $T_{\max}$, and $T_{\min}$ calculated respectively from (1), (6), and (7), which are plotted as a function of (a) f ($\theta = 0$) and (b) θ ($f = 270$ GHz). ($t = 10$ mm and $\varepsilon_{\mathrm{r}} = 3 - j0.01$.)

$$|S_{11}|^2 = \frac{|\Gamma|^2\left[1+\exp\left(4\beta^{\mathrm{i}}\right)-2\exp\left(2\beta^{\mathrm{i}}\right)\cos\left(2\beta^{\mathrm{r}}\right)\right]}{1+|\Gamma|^4\exp\left(4\beta^{\mathrm{i}}\right)-2|\Gamma|^2\exp\left(2\beta^{\mathrm{i}}\right)\cos\left(2\beta^{\mathrm{r}}\right)}. \quad (10)$$

Since (10) obviously takes maximal and minimal values respectively when $\beta^{\mathrm{r}} = (2m+1)\pi/2$ and $\beta^{\mathrm{r}} = m\pi$, the maximal and minimal envelopes of $|S_{11}|^2$ are written as

$$R_{\max} = \frac{|\Gamma|^2\left[1+\exp\left(2\beta^{\mathrm{i}}\right)\right]^2}{\left[1+|\Gamma|^2\exp\left(2\beta^{\mathrm{i}}\right)\right]^2}, \quad (11)$$

$$R_{\min} = \frac{|\Gamma|^2\left[1-\exp\left(2\beta^{\mathrm{i}}\right)\right]^2}{\left[1-|\Gamma|^2\exp\left(2\beta^{\mathrm{i}}\right)\right]^2}. \quad (12)$$

Note that similar to (5), (6), and (7), three of these equations, (10), (11), and (12), are a function of the frequency f or the

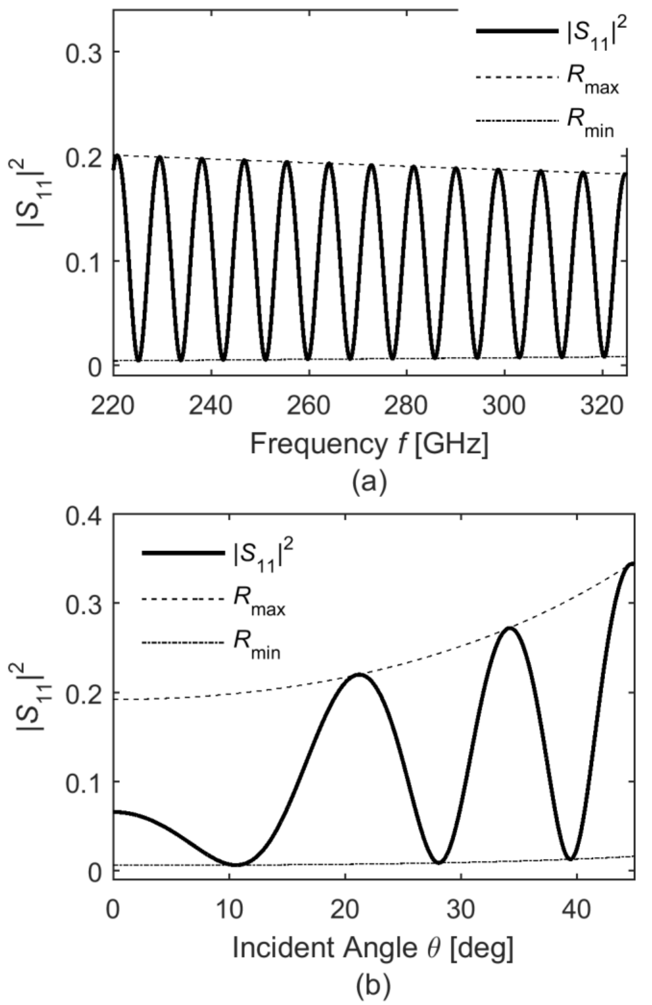

Fig. 3. $|S_{11}|^2$, $R_{\max}$, and $R_{\min}$ calculated respectively from (1), (6), and (7), which are plotted as a function of (a) f ($\theta = 0$) and (b) θ ($f = 270$ GHz). ($t = 10$ mm and $\varepsilon_r = 3 - j0.01$.)

angle θ (see Fig.3 (a) and (b) for illustrative plots of $|S_{11}|^2$, $R_{\max}$, and $R_{\min}$). In addition, from (11) and (12), we get

$$|\Gamma| = \frac{1+\sqrt{R_{\max}R_{\min}} \pm \sqrt{1-R_{\max}-R_{\min}+R_{\max}R_{\min}}}{\sqrt{R_{\max}}+\sqrt{R_{\min}}}, \tag{13}$$

$$|\Gamma|\exp\left(2\beta^{\mathrm{i}}\right) = \frac{1-\sqrt{R_{\max}R_{\min}} \pm \sqrt{1-R_{\max}-R_{\min}+R_{\max}R_{\min}}}{\sqrt{R_{\max}}-\sqrt{R_{\min}}}. \tag{14}$$

Note that the signs in (13) and (14) should be chosen so that $|\Gamma| \le 1$ and $0 < \exp\left(\beta^{\mathrm{i}}\right) \le 1$, and that Γ is mostly $\Gamma \le 0$ for the same reason as for Γ obtained from (9) with (8).

In this paper, our scattering measurement system employs an illumination of a transverse-electric (TE) polarized wave. In that event, the reflection coefficient Γ is given by the Fresnel relation that is a function of the incident angle θ and the permittivity ε_r of the material as follows.

$$\Gamma = \frac{\cos\theta - \sqrt{\varepsilon_r - \sin^2\theta}}{\cos\theta + \sqrt{\varepsilon_r - \sin^2\theta}}. \tag{15}$$

Equation (15) allows us to in turn calculate ε_r from Γ obtained either from (8) and (9) with S_{21} measurement data or from (13) when S_{11} is measured, in such a way that

$$\varepsilon_r = \varepsilon_r' - j\varepsilon_r'' = \left(\frac{1-\Gamma}{1+\Gamma}\right)^2 \cos^2\theta + \sin^2\theta. \tag{16}$$

Note here that it has been assumed that a low-loss dielectric material ($\varepsilon_r' \gg \varepsilon_r''$) is measured and that (16) produces the real part of the permittivity, $\varepsilon_r \cong \varepsilon_r'$.

In order to make free-space bidirectional scattering measurements and apply the method derived above to extracting the permittivity, the VNA is employed that has a finite dynamic range and that may not be able to measure very small scattering parameters. In the case when we measure a low-loss dielectric material, the minimal $|S_{11}|^2$ can be too small to acquire an accurate minimal $|S_{11}|^2$ envelope, $R_{\min}$. Accordingly, we use S_{21} measurement data rather than S_{11} data as to extract ε_r' throughout this work. It should be also noted that since we can have more numbers of maximal and minimal peaks of $|S_{21}|^2$ as a function of frequency than those as a function of incident angle (see Figs. 2), we use $|S_{21}|^2$ as a function of frequency rather than incident angle in this paper. Moreover, we smooth out $|S_{21}|^2$ measurement data to remove extraneous small noises and contaminations, and we employ the numerical interpolation technique for approximating the maximal and minimal envelopes $T_{\max}$ and $T_{\min}$.

B. Determining the Sample Thickness t

The sample thickness t is calculated with ε_r' and the frequencies for maximal and minimal $|S_{21}|^2$ as follows.

$$t = \frac{1}{N-1}\sum_{m=1}^{N-1}\frac{c}{4\left(F_{m+1}-F_m\right)\sqrt{\varepsilon_{\mathrm{r,ave}}' - \sin^2\theta}}, \tag{17}$$

where N is the number of maximal and minimal $|S_{21}|^2$, c is the speed of light in the air, F_m is the frequency for the maximal and minimal peaks, and $\varepsilon_{\mathrm{r,ave}}'$ is the average ε_r' over each interval between the frequencies, $F_1, F_2, \ldots, F_N$, for maximal and minimal $|S_{21}|^2$ (see Fig. 4).

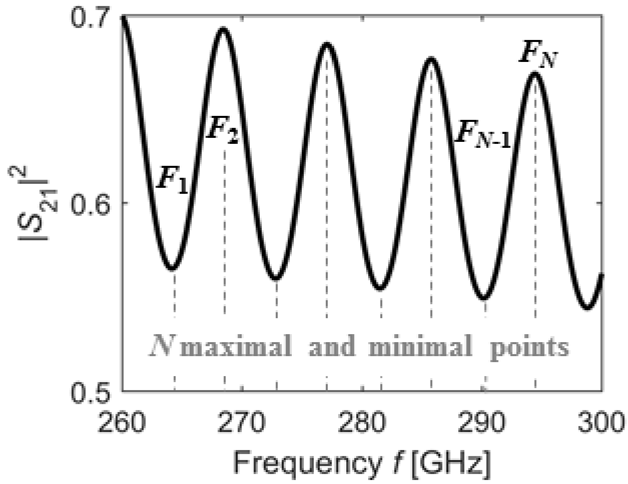

Fig. 4. Maximal and minimal $|S_{21}|^2$. ($\theta = 0$, $t = 10$ mm and $\varepsilon_r = 3 - j0.01$.)

C. *Equations for Extracting* ε_r''

Once we achieve $\varepsilon_{\mathrm{r}}'$, $\exp(\beta^{\mathrm{i}})$, and t using the method described in subsections II-A and II-B, it is simple and straightforward to calculate the imaginary part $\varepsilon_{\mathrm{r}}''$.

An assumption that the real part of the permittivity is substantially larger than the imaginary part, i.e., $\varepsilon_{\mathrm{r}}' - \sin^2\theta \gg \varepsilon_{\mathrm{r}}''$, leads (3) to

$$\beta = \beta^{\mathrm{r}} + j\beta^{\mathrm{i}} = \frac{2\pi t}{\lambda_0}\sqrt{\varepsilon_{\mathrm{r}}' - \sin^2\theta}\left[1 - j\frac{\varepsilon_r''}{2\left(\varepsilon_{\mathrm{r}}' - \sin^2\theta\right)}\right]. \tag{18}$$

By grouping the real and imaginary parts and separating β^{r} and β^{i} in (18), it follow that

$$\varepsilon_{\mathrm{r}}'' = -\frac{\lambda_0\beta^{\mathrm{i}}}{\pi t}\sqrt{\varepsilon_{\mathrm{r}}' - \sin^2\theta}, \tag{19}$$

where β^{i} is calculated with (8) or with (13) and (14)—we do not make use of (13) and (14) since we utilize only S_{21} measurement data in this paper. Note that when calculating β^{i} by taking the natural logarithm of $\exp(\beta^{\mathrm{i}})$ from (8), there should not be any ambiguity of the branch cut because β^{i} is real-valued.

D. *Uncertainties for* ε_r' *and* ε_r''

The thorough evaluation of uncertainties in the extracted permittivity needs to include not only systematic errors in measurement quantities but also effects due to the interpolation technique for approximating the maximal and minimal envelopes of $|S_{21}|^2$. However, it is very challenging to derive analytical uncertainties for extracted $\varepsilon_{\mathrm{r}}'$ and $\varepsilon_{\mathrm{r}}''$ that accounts for the uncertainty in the interpolation for the maximal and minimal envelopes. At present stage, it is postulated that sources of the uncertainties are systematic errors in $T_{\max}$, $T_{\min}$, θ, and t, and we will investigate effects of the interpolation for the envelopes on measurements in section IV. All of the errors in $T_{\max}$, $T_{\min}$, θ, and t are also assumed to be independent although in most cases this is a weak assumption. The uncertainty analysis is performed separately for $\varepsilon_{\mathrm{r}}'$ and $\varepsilon_{\mathrm{r}}''$ in the following.

The differential uncertainty is applicable to $\varepsilon_{\mathrm{r}}'$, and the total uncertainty of $\varepsilon_{\mathrm{r}}'$ is expressed with

$$\Delta\varepsilon_{\mathrm{r}}' = \sqrt{\left(\frac{\partial\varepsilon_{\mathrm{r}}'}{\partial\Gamma}\Delta\Gamma\right)^2 + \left(\frac{\partial\varepsilon_{\mathrm{r}}'}{\partial\theta}\Delta\theta\right)^2}, \tag{20}$$

where the derivatives can be explicitly calculated as

$$\frac{\partial\varepsilon_{\mathrm{r}}'}{\partial\Gamma} = -\frac{4(1-\Gamma)}{(1+\Gamma)^3}\cos^2\theta, \tag{21}$$

$$\frac{\partial\varepsilon_{\mathrm{r}}'}{\partial\theta} = (\sin 2\theta)\left[1 - \left(\frac{1-\Gamma}{1-\Gamma}\right)^2\right]. \tag{22}$$

In (20), $\Delta\Gamma$ is a function of $T_{\max}$, $T_{\min}$, $\Delta T_{\max}$, and $\Delta T_{\min}$ where $\Delta T_{\max}$ and $\Delta T_{\min}$ are the measurement bounds obtained from specifications of the VNA (for the explicit expression for $\Delta\Gamma$, see Appendix), and $\Delta\theta$ is the systematic error estimated from repeated measurements by rotating the goniometric sample stage to vary the incident angle.

The total differential uncertainty of $\varepsilon_{\mathrm{r}}''$ is represented by

$$\Delta\varepsilon_{\mathrm{r}}'' = \sqrt{\left(\frac{\partial\varepsilon_{\mathrm{r}}''}{\partial\beta^{\mathrm{i}}}\Delta\beta^{\mathrm{i}}\right)^2 + \left(\frac{\partial\varepsilon_{\mathrm{r}}''}{\partial t}\Delta t\right)^2 + \left(\frac{\partial\varepsilon_{\mathrm{r}}''}{\partial\varepsilon_{\mathrm{r}}'}\Delta\varepsilon_{\mathrm{r}}'\right)^2 + \left(\frac{\partial\varepsilon_{\mathrm{r}}''}{\partial\theta}\Delta\theta\right)^2}, \tag{23}$$

where

$$\Delta\beta^{\mathrm{i}} = \Delta\chi/\chi, \tag{24}$$

with

$$\chi = \exp(\beta^{\mathrm{i}}). \tag{25}$$

The derivatives in (23) can be explicitly expressed with

$$\frac{\partial\varepsilon_{\mathrm{r}}''}{\partial\beta^{\mathrm{i}}} = -\frac{\lambda_0}{\pi t}\sqrt{\varepsilon_{\mathrm{r}}' - \sin^2\theta}, \tag{26}$$

$$\frac{\partial \varepsilon_r''}{\partial t} = \frac{\lambda_0 \beta^i}{\pi t^2}\sqrt{\varepsilon_r' - \sin^2\theta}, \tag{27}$$

$$\frac{\partial \varepsilon_r''}{\partial \varepsilon_r'} = -\frac{\beta^i \lambda_0}{2\pi t\sqrt{\varepsilon_r' - \sin^2\theta}}, \tag{28}$$

$$\frac{\partial \varepsilon_r''}{\partial \theta} = \frac{\beta^i \lambda_0 \sin 2\theta}{2\pi t\sqrt{\varepsilon_r' - \sin^2\theta}}. \tag{29}$$

In (23), Δt is estimated from repeated measurements with (17), and $\Delta\varepsilon_r'$ is generated by (20). In (24), $\Delta\chi$ is a function of T_{max}, T_{min}, ΔT_{max}, and ΔT_{min}. For the explicit expression for $\Delta\chi$, see Appendix.

III. Measurement System

At NIST, we previously developed the bidirectional scattering measurement system that permits simultaneous monostatic and bistatic measurements with one setup [21]. The system was originally intended to measure BRDFs of various materials and small objects and to provide reference quality data in the frequency range of 200-500 GHz. The system also proved capable of semi-two-port scattering parameter (S_{11}, S_{22}, and S_{21}) measurements for materials.

Fig. 5 shows a photograph of the bidirectional scattering measurement system at NIST. In Fig. 5, the measurement system is constructed with a transmitter, receiver, sample and receiver rotators, and VNA. Each of the transmitter and receiver consists of a frequency converter and antenna. In this paper, the converters operate at 220-325 GHz, and the antennas are standard WR-03 horns. The sample rotator is installed on the top of an *x-y* translation stage, and the top of the sample rotator is equipped with a goniometric stage a sample holder can be directly attached to. The transmitter and receiver are placed on the two-axis, tilt-and-rotation platform sitting on *x-y* translation stages. Lenses are mounted at a slide optical pole on an optical rail. These mechanical configurations allow us to very accurately level and fully align the entire measurement system.

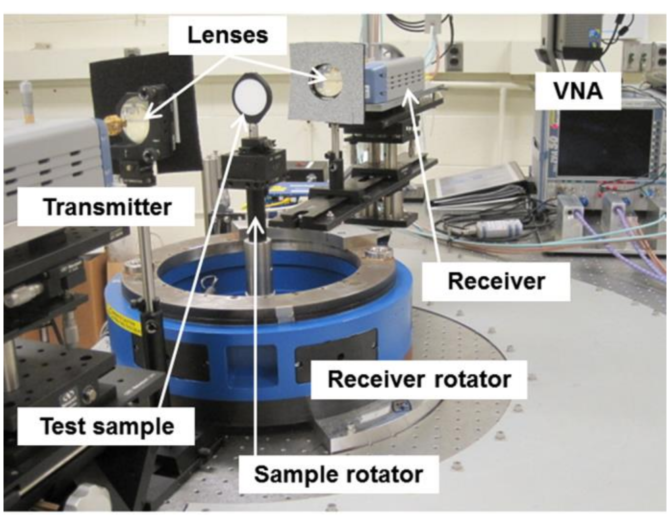

Fig. 5. Photograph of the bidirectional scattering measurement system at NIST.

In this paper, the distance between the antennas is approximately 70 cm, and the distance between the lenses is about 50 cm. The lenses are positioned to maximize the collimation of the illumination beam. In this measurement configuration for the focused beam, the depth of focus is estimated to be nearly 20 cm, and the half beam width about 10-20 mm at 220-325 GHz.

Although we use the magnitude only of S_{21} to extract the permittivity and the sample thickness, we make the semi-two-port (one-path, two-port) calibration as was done in [21]. To this end, we first performed an open-short-load (OSL) calibration without the horn antennas, lenses, and a sample for S_{11} and S_{22} measurements, and as well a free-space thru calibration without the sample but with the horn antennas and lenses for S_{21} measurements. Consecutively, we made scattering parameter measurements for test samples introduced into the sample fixture between the antennas, and then normalized S_{21} by S_{21} measured without the sample prior to extracting material properties from S_{21} measured for the samples. Note that although only S_{21} was necessary to calculate ε_r', t, and ε_r'', S_{11} was also measured with a mirror to validate the equipment levels, alignments, etc. In addition, we utilized the time-gating function of the VNA to smooth out measured S-parameters by removing measurement contaminations arising from multiple reflections between the two antennas and between the sample and the antenna. We made all scattering parameter measurements at the laboratory where the temperature was adequately stabilized to about 18℃ to minimize drift of the VNA measurements and property change of the materials due to temperature variation.

IV. Results and Discussion

To test out the free-space measurement method outlined above, three different low-loss materials, cross-linked polystyrene (XLPS), polytetrafluoroethylene (PTFE), and polymethylpentene (PMP), were measured as test samples. These materials were machined to the disk shape of approximately 50.8 mm in diameter so that these samples could be accommodated into the sample fixture. Two XLPS samples of different thickness, one PTFE sample, and one PMP sample were prepared. Our method for extracting properties of the materials only requires the samples have parallel-plate faces.

To make scattering parameter measurements on test samples, we used the measurement system described in section III. During the measurements, all movements of the rotators were fully automated by the NIST-developed in-house software, and controlled with precision of ± 0.01 degrees.

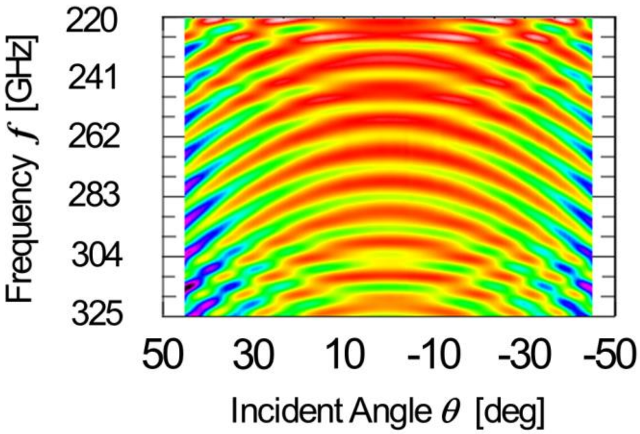

Fig. 6. Contour plot of $|S_{21}|^2$ measured for XLPS sample 1 as a function of both of frequency and incident angle.

Fig. 6 shows the contour plot of the magnitude of S_{21} measured for one of the XLPS samples (XLPS sample 1) as a function of frequency and incident angle. It is seen that compared to S_{21} from the theoretical calculation for an infinitely large disk of the sample (the plot for the theoretical calculation is not shown to save the number of pages), the measured S_{21} starts to deviate from the theoretical S_{21} as the incident angle goes 35 degrees or beyond (or -35 degrees or less). It is deduced that the illumination upon the actual samples is clipped by the frame of the sample fixture at 35 degrees or beyond (or -35 degrees or less). Thus, in this paper, we use S_{21} measured at 0, 10, 20, and 30 degrees to characterize properties of the materials.

Figs. 7(a)-(d) show the magnitudes of S_{21} measured for XLPS sample 1 as a function frequency, and those are plotted for the incident angles of 0, 10, 20, and 30 degrees. These $|S_{21}|^2$ curves are smoothed out to eliminate extraneous small noises. Figs. 7(a)-(d) also represent maximal and minimal peaks found from the smoothed curves by searching for local maxima and minima of the curves. To appropriately determine the maximal and minimal envelopes of $|S_{21}|^2$, we attempted to investigate four different kinds of interpolations: the smoothing spline fitting, the linear interpolation, the piecewise cubic interpolation, and the fast Fourier transform (FFT) approximation, all of which approximate the envelopes of $|S_{21}|^2$ (for details about these computational algorithms, see MATLAB† documents [22]). It is observed in these plots that, in general, the smoothing spline fitting best approximates the envelopes whereas the FFT approximation appears most oscillatory. Hence, in this paper, the smoothing spline fitting is used to obtain the maximal and minimal envelopes of $|S_{21}|^2$ to extract the permittivity. In addition, we discard peaks that are

† Reference to specific software is provided only for informational purposes and does not constitute any endorsement by the National Institute of Standards and Technology.

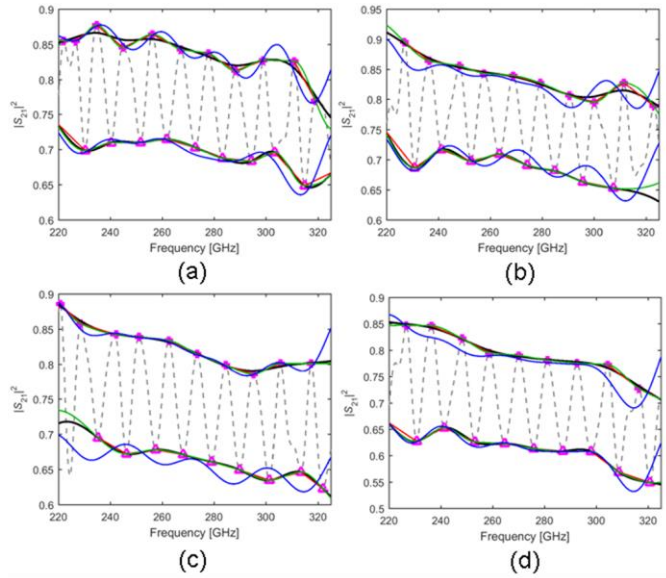

Fig. 7. $|S_{21}|^2$ measured for XLPS sample1 at (a) 0 degree, (b) 10 degrees, (c) 20 degrees, and (d) 30 degrees. The dashed gray lines represent measured $|S_{21}|^2$, and the pink cross and triangle symbols represent maximal and minimal peaks, respectively. The solid black, red, green, and blue lines represent the smoothing spline fitting, linear interpolation, piecewise cubic interpolation, and FFT approximation, respectively.

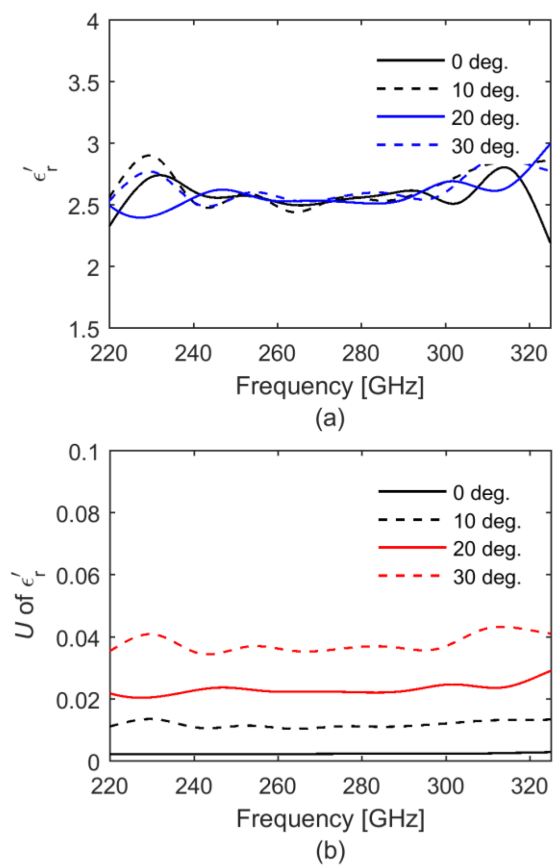

Fig. 8. (a) Real part ε_r' of the permittivity, and (b) the expanded uncertainty U of ε_r' for XLPS sample 1 ($k=2$).

TABLE I
SAMPLE THICKNESS CALCULATED FROM (17)

Incident angle θ	XLPS sample 1	XLPS sample 2	PTFE sample	PMP sample
0 deg.	8.90 mm	9.94 mm	10.71 mm	9.93 mm
10 deg.	8.79 mm	9.91 mm	10.42 mm	10.25 mm
20 deg.	9.03 mm	10.05 mm	10.03 mm	10.11 mm
30 deg.	8.75 mm	9.81 mm	10.03 mm	10.22 mm

evidently anomalous or greater than unity.

Fig. 8(a) shows ε_r' calculated from (16) for XLPS sample 1 at incident angles, 0, 10, 20, and 30 degrees. In Fig. 8(a), it is seen that ε_r' for all incident angles converges to exactly about 2.5 in the frequency range of 235-308 GHz where there exist sufficient pairs of the maximal and minimal peaks. Furthermore, large discrepancies with $\varepsilon_r' \cong 2.5$ around the start and end frequencies is speculated to be attributed to an alias phenomenon originating from the time gating of the VNA used for S_{21} measurements.

Fig. 8(b) shows the expanded uncertainty in the extracted ε_r' for XLPS sample 1 at incident angles, 0, 10, 20, and 30 degrees. The expanded uncertainty is defined as $U = ku_c$ where k is the coverage factor, and u_c is the standard uncertainty ($\Delta\varepsilon_r'$ or $\Delta\varepsilon_r''$ in this paper). For example, if the normal distribution as assumed for Type B evaluation applies to u_c and the coverage factor is chosen to be $k = 2$, then the expanded uncertainty U gives an interval with a level of confidence of approximately 95% [23, 24]. To calculate the expanded uncertainty U, we used the coverage factor $k = 2$, $\Delta T_{\max}, \Delta T_{\min} = \pm 10^{-4}$ corresponding to a -40 dB dynamic range of the VNA, and $\Delta\theta = \pm 0.01$ degrees. The uncertainty should be customarily reported in the form of $\pm U$ rather than its absolute value (see [23, 24]). From Fig. 8(b), it is confirmed that the uncertainty gets larger as the incident angle gets larger whereas minimum uncertainty occurs to $\theta = 0$. Again note here that the uncertainty plotted in Fig. 8(b) does not include the interpolation for the envelopes.

Table I lists the thickness t of XLPS sample 1 calculated from (17). For calculating t with (17), we choose the frequency range from 240-300 GHz, because measurement data around the mid-band seem to be reliable, in that, near the start and end frequencies, there is absence of maximal and minimal peaks that enables good interpolations and the alias present, as mentioned above about ε_r' obtained with the present method. The thickness t of XLPS sample 1 listed in Table I exhibits a variation from 8.75 mm to 9.03 mm. For comparison, t was measured with a micrometer, coming up with $t = 8.83$ mm. It gives an observation that the sample thickness t from (17) yields nominal errors within about $\pm 2\%$.

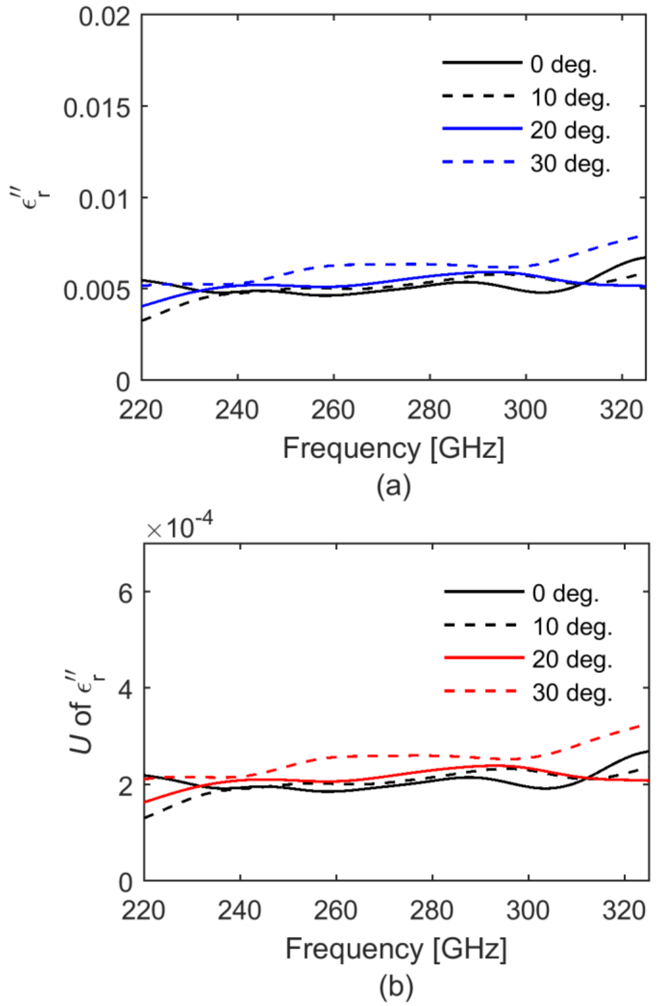

Fig. 9. Imaginary part ε_r'' of the permittivity, and (b) the expanded uncertainty U of ε_r'' for XLPS sample 1 ($k = 2$).

Fig. 9(a) shows ε_r'' obtained from (19) for XLPS sample 1 at incident angles, 0, 10, 20, and 30 degrees. It is seen in Fig. 9(a) that ε_r'' for all incident angles converges around $\varepsilon_r'' = 0.005$ and that discrepancies among ε_r'' at different incident angles get large around the start and end frequencies. Fig. 9(b) shows the expanded uncertainty $U = k\Delta\varepsilon_r''$ in the extracted ε_r'' for XLPS sample 1 at incident angles, 0, 10, 20, and 30 degrees. We used $k = 2$, $\Delta T_{\max}, \Delta T_{\min} = \pm 10^{-4}$, $\Delta\theta = \pm 0.01$ degrees, and $\Delta t = \pm 2\%$ in (23). It is seen in Fig. 9(b) that the expanded uncertainty in ε_r'' at all incident angles is estimated to be nearly $2 \cdot 10^{-4}$.

In addition, we measured another XLPS sample (XLPS sample 2) of different length than that of XLPS sample 1, and PTFE and PMP samples. Figs. 10, 11, and 12 show calculated ε_r', ε_r'', and their expanded uncertainties U for XLPS sample 2, PTFE and PMP samples, respectively. We extracted these

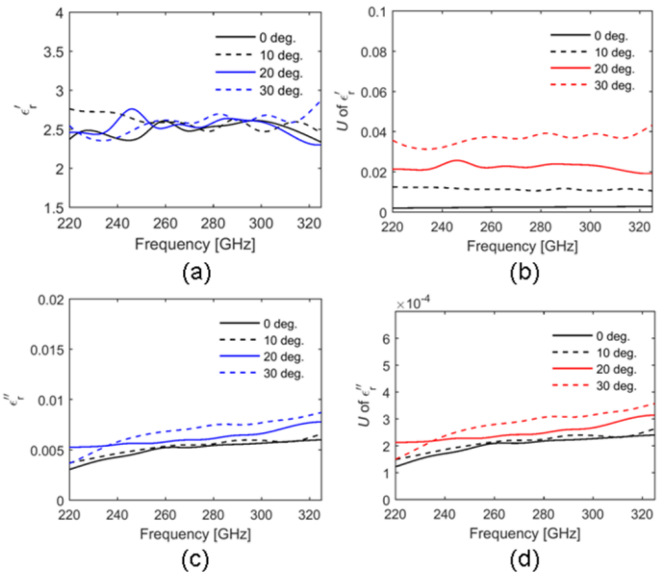

Fig. 10. (a) ε_r', (b) U of ε_r', (c) ε_r'', and (d) U of ε_r'' for XLPS sample 2.

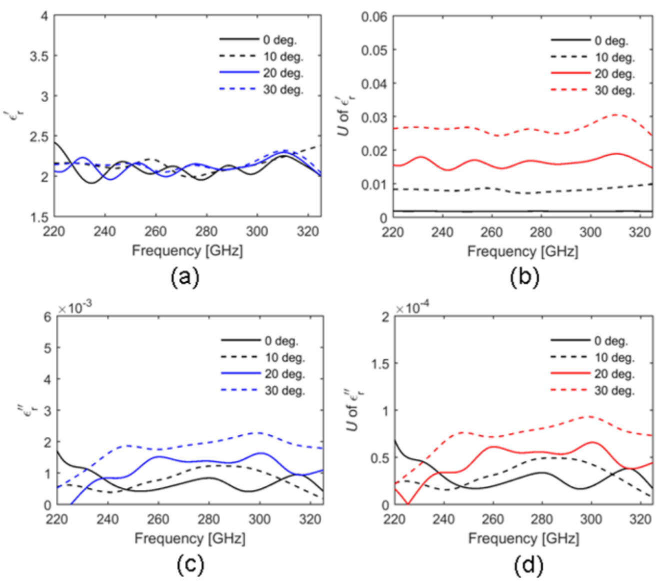

Fig. 11. (a) ε_r', (b) U of ε_r', (c) ε_r'', and (d) U of ε_r'' for the PTFE sample.

properties in the same manner as was done for XLPS sample 1. The thickness t of these samples are given in Table I. To calculate t, the frequency range from 240-300 GHz was chosen for exactly the same reason for the case of XLPS sample 1. To calculate the expanded uncertainties, we used $k=2$, and input the same systematic errors, $\Delta T_{max}, \Delta T_{min} = \pm 10^{-4}$, $\Delta\theta = \pm 0.01$ degrees, and $\Delta t = \pm 2\,\%$ as was done for the case of XLPS sample 1.

In Figs 10(a) and (c), ε_r' and ε_r'' of XLPS sample 2 are approximately 2.5 and 0.005 as was observed for XLPS sample 1. It is seen in Figs. 10(b) and (d) that similar to XLPS sample 1, the expanded uncertainty U in ε_r' increases with the

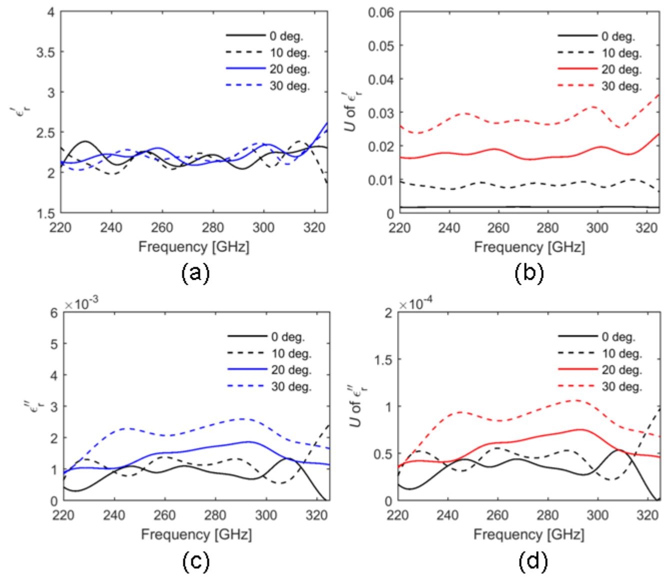

Fig. 12. (a) ε_r', (b) U of ε_r', (c) ε_r'', and (d) U of ε_r'' for the PMP sample.

incident angle θ being large whereas U in ε_r'' relatively converges around $2\cdot 10^{-4}$. The thickness t listed in Table I varies from 9.81 mm to 10.05 mm, which generates approximately $\Delta t = \pm 2$ % compared to the value of 10.02 mm the micrometer measured to be.

Figs. 11 and 12 show the permittivity ε_r' and ε_r'' and the expanded uncertainties U extracted for the PTFE and PMP samples, respectively. The thickness t for all incident angles is listed in Table I. We used measurement data in the frequency range from 240-300 GHz to obtain t, and used $k=2$, $\Delta T_{max}, \Delta T_{min} = \pm 10^{-4}$, $\Delta\theta = \pm 0.01$ degrees, and $\Delta t = \pm 2$ % to calculate the uncertainties. ε_r' plotted in Fig. 11(a) and Fig. 12 (a) for the PTFE and PMP samples are approximately $\varepsilon_r' = 2.0$ to 2.1 and $\varepsilon_r' = 2.1$ to 2.2, respectively. The expanded uncertainties U in ε_r' for each sample are shown to increase with θ being increased. The thickness t of these samples for all angles is given in Table I, indicating a variation that yields an error about $\pm 2\%$ in comparison to the values of 9.99 mm and 10. 02 mm the micrometer read respectively for the PTFE and PMP samples. The imaginary part ε_r'' plotted in Fig. 11(c) and Fig. 12(c) indicates lower loss than those of the XLPS samples. It is seen in Fig. 11(d) and Fig. 12(d) that the expanded uncertainties U in ε_r'' for each of samples turn out to be smaller than those of the XLPS samples.

V. Conclusion

The free-space measurement method for low-loss dielectric characterizations has been developed without any assumption of *a priori* knowledge of the sample thickness. First, we have formulated the equations for ε_r' obtained from the maximal and minimal envelopes, T_{max} and T_{min}, of measured $|S_{21}|^2$ and the equations for ε_r' from the maximal and minimal envelopes, R_{max} and R_{min}, of measured $|S_{11}|^2$. The thickness t has been then estimated from the average permittivity $\varepsilon_{r,ave}'$ and the frequencies, $F_1, F_2, ..., F_N$, for $|S_{21}|^2$ peaks, and ε_r'' has been calculated with ε_r' and t. In addition, the explicit expressions for the uncertainties in ε_r' and ε_r'' have been also derived. Because more maximal and minimal peaks are observed as a function of frequency than as a function of incident angle, the scattering parameters for the test materials have been measured as a function of frequency. Moreover, we have utilized S_{21} measurement data since minimal peaks of $|S_{11}|^2$ for low-loss dielectric measurements can be too small to accurately measure R_{min} due to the finite dynamic range of the VNA.

To test out the present method, four dielectric samples (XLPS sample 1, XLPS sample 2, PTFE sample, and PMP sample) have been measured at 220-325 GHz at 0, 10, 20, and 30 degrees. It has been observed from the measurements for XLPS samples 1 and 2 that ε_r' for all incident angles converges to approximately 2.5 around at 235-308 GHz whereas large discrepancies $\varepsilon_r' \cong 2.5$ near the start and end frequencies have been seen that stem from paucity of sufficient maximal and minimal peaks and from the alias arising from the time-gating of the VNA. The thickness t of the XLPS samples that was estimated from 240 GHz to 300 GHz has turned out to be within approximately $\pm 2\%$ error, and ε_r'' for the samples was found to be about 0.005. It has been also confirmed that the minimum uncertainty in ε_r' occurs to $\theta = 0$.

From the measurements for the PTFE and PMP samples, it has been validated that the real parts of the permittivity are $\varepsilon_r' = 2.0$ to 2.1 and $\varepsilon_r' = 2.1$ to 2.2, respectively, and the thickness t is calculated with about $\pm 2\%$ error, and that the imaginary parts are much smaller than those of the XLPS samples. In addition, it has been confirmed that the uncertainties in their ε_r' increases with θ being increased, similar to the measurement cases of XLPS samples 1 and 2.

It is predicted that it is generally problematic to know the sample thickness precise enough to extract the permittivity with the conventional free-space measurement method at very high frequencies, and that the present method that does not need *a priori* of the knowledge of the thickness will be considerably beneficial to measure ε_r' at very high frequencies.

In addition, the present method has been examined with isotropic dielectric materials. However, if there should exist any anisotropic materials, the present method will be applicable to those materials by switching the polarization between transverse-electric (TE) and transverse-magnetic (TM) polarizations and by varying the incident angle.

Appendix

The uncertainty $\Delta\Gamma$ in the reflection coefficient is given by

$$\Delta\Gamma = \sqrt{\left(\frac{\partial\Gamma}{\partial T_{max}}\Delta T_{max}\right)^2 + \left(\frac{\partial\Gamma}{\partial T_{min}}\Delta T_{min}\right)^2 + \left(\frac{\partial\Gamma}{\partial\chi}\Delta\chi\right)^2}, \tag{30}$$

where the derivative are explicitly obtainable as

$$\begin{aligned}\frac{\partial\Gamma}{\partial T_{max}} &= \frac{1}{2\Gamma\left(\sqrt{T_{max}}+\sqrt{T_{min}}\right)\chi^2}\\ &\cdot\left[\frac{\sqrt{T_{min}/T_{max}}}{\sqrt{T_{max}}+\sqrt{T_{min}}} - 2\frac{\sqrt{T_{max}}-\sqrt{T_{min}}}{\chi}\left(\frac{\partial\chi}{\partial T_{max}}\right)\right],\end{aligned} \tag{31}$$

$$\begin{aligned}\frac{\partial\Gamma}{\partial T_{min}} &= -\frac{1}{2\Gamma\left(\sqrt{T_{max}}+\sqrt{T_{min}}\right)\chi^2}\\ &\cdot\left[\frac{\sqrt{T_{max}/T_{min}}}{\sqrt{T_{max}}+\sqrt{T_{min}}} + 2\frac{\sqrt{T_{max}}-\sqrt{T_{min}}}{\chi}\left(\frac{\partial\chi}{\partial T_{min}}\right)\right].\end{aligned} \tag{32}$$

The uncertainty $\Delta\chi$ in $\chi = \exp\left(\beta^{i}\right)$ is written as

$$\Delta\chi = \sqrt{\left(\frac{\partial\chi}{\partial T_{max}}\Delta T_{max}\right)^2 + \left(\frac{\partial\chi}{\partial T_{min}}\Delta T_{min}\right)^2}, \tag{33}$$

where the derivatives are

$$\begin{aligned}\frac{\partial\chi}{\partial T_{max}} &= \frac{1}{2\sqrt{T_{max}+T_{min}}}\left(\frac{T_{min}}{\sqrt{T_{max}T_{min}}} + \frac{T_{min}+1}{\sqrt{T_{max}-T_{min}+T_{max}T_{min}}}\right)\\ &-\frac{\sqrt{T_{max}T_{min}}+\sqrt{T_{max}-T_{min}+T_{max}T_{min}}}{2\left(\sqrt{T_{max}}+\sqrt{T_{min}}\right)^2\sqrt{T_{max}}},\end{aligned} \tag{34}$$

$$\begin{aligned}\frac{\partial\chi}{\partial T_{min}} &= \frac{1}{2\sqrt{T_{max}+T_{min}}}\left(\frac{T_{max}}{\sqrt{T_{max}T_{min}}} + \frac{T_{max}-1}{\sqrt{T_{max}-T_{min}+T_{max}T_{min}}}\right)\\ &-\frac{\sqrt{T_{max}T_{min}}+\sqrt{T_{max}-T_{min}+T_{max}T_{min}}}{2\left(\sqrt{T_{max}}+\sqrt{T_{min}}\right)^2\sqrt{T_{min}}}.\end{aligned} \tag{35}$$

Acknowledgment

This work was supported in part by Los Alamos National Laboratory (LANL), Albuquerque, NM, USA.

References

[1] G. L. Matthaei, L. Young, and E. M. Jones, *Microwave Filters, Impedance-Matching Networks, and Coupling Structures*. Northwood MA: Artech House, 1980.

[2] I. Bahl and P. Bhartia, *Microwave Solid Sate Circuit Design*, 2nd Ed. Hoboken NJ: Wiley, 2003.
[3] J. Baker-Jarvis, M. D. Janezic, and D. C. DeGroot, "High-frequency dielectric measurements," *IEEE Instrum. Meas. Mag.*, Vol. 13, no. 2, pp. 24-31, Apr. 2010.
[4] L. F. Chen, C. K. Ong, C. P. Neo, V. V. Varadan, and V. K. Varadan, *Microwave Electronics: Measurement and Materials Characterisation.* West Sussex, England: Wiley, 2004.
[5] R. M. Redheffer, "The measurement of dielectric constants," in *Technique of Microwave Measurements*, C. G. Montgomery, Ed. NY: McGraw-Hill, 1947.
[6] K. H. Breeden, "Error analysis for waveguide-bridge dielectric-constant measurements at millimeter wavelengths," *IEEE Trans. Instrum. Meas.*, Vol. 18, no. 3, pp. 203-209, Sep. 1969.
[7] C. K. Campbell, "Free-space permittivity measurements on dielectric materials at millimeter wavelengths," *IEEE Trans. Instrum. Meas.*, Vol. 27, no. 1, pp. 54-58, Mar. 1978.
[8] D. K. Ghodgaonkar, V. V. Varadan, and V. K. Varadan, "A free-space method for measurement of dielectric constants and loss tangent at microwave," *IEEE Trans. Instrum. Meas.*, Vol. 37, no. 3, pp. 789-793, Jun. 1989.
[9] V. V. Varadan, R. D. Richard, D. K. Ghodgaonkar, and V. K. Varadan, "Free-space, broadband measurements of high temperature, complex dielectric properties at microwave frequencies," *IEEE Trans. Instrum. Meas.*, Vol. 40, no. 5, pp. 842-846, Oct. 1991.
[10] D. K. Ghodgaonkar, V. V. Varadan, and V. K. Varadan, "Free-space measurement of complex permittivity and complex permeability of magnetic materials at microwave frequencies," *IEEE Trans. Instrum. Meas.*, Vol. 39, no. 2, pp. 387-394, Apr. 1990.
[11] G. L. Friedsam and E. M. Biebl, "A broadband free-space dielectric properties measurement system at millimeter wavelengths," *IEEE Trans. Instrum. Meas.*, Vol. 46, no. 2, pp. 515-518, Apr. 1997.
[12] T. Tosaka, K. Fujii, K. Fukunaga, and A. Kasamitsu, "Development of complex relative permittivity measurement system based in free-space in 220−330-GHz range," *IEEE Trans. THz Sci. Technol.*, Vol. 5, no. 1, pp. 102-109, Jan. 2015.
[13] D. A. Minkov, "Method for determining the optical constants of a thin film on a transparent substrate," *J. Phys. D: Appl. Phys*. Vol. 22, no. 1, pp. 199-205, Jan. 1989.
[14] D. A. Minkov, "Calculation of the optical constants of a thin layer upon a transparent substrate from the reflection spectrum," *J. Phys. D: Appl. Phys.* Vol. 22, no. 8, pp. 1157-1161, Aug. 1989.
[15] V. V. Filippov, "Method of the ratio of envelopes of the reflection spectrum for measuring optical constants and thickness of thin films," *Opt. Spectr.*, Vol. 88, no. 4, pp. 641-646, Apr. 2000.
[16] V. P. Kutavichus, V. V. Filippov, and V. H. Huzouski, "Determination of optical parameters and thickness of weakly absorbing thin films from reflectance and transmittance spectra," *Appl. Opt.*, Vol. 45, no. 19, pp. 4547-4553, Jul. 2006.
[17] A. M. El-Naggar, S. Y. El-Zaiat, and S. M. Hassan, "Optical parameters of epitaxial GaN thin film on Si substrate from the reflection spectrum," *Opt. Laser Technol.*, Vol. 41, no.3, pp. 334-338, Apr. 2009.
[18] R. Swanepoel, "Determination of surface roughness and optical constants of inhomogeneous amorphous silicon films," *J. Physics E: Scientific Instrument*, Vol. 17, no. 10, pp. 896-903, Oct. 1984.
[19] J. C. Martínez-Antón, "Determination of optical parameters in general film-substrate systems: a reformulation based on the concepts of envelope extremes and local magnitudes," *Appl. Opt.*, Vol. 39, no. 25, pp. 4557-4568, Sep. 2000.
[20] S.-T. Yen and P.-K. Chung, "Extraction of optical constants from maxima of fringing reflectance spectra," *Appl. Opt.*, Vol. 54, no. 4, pp. 663-668, Feb. 2015.
[21] D. Novotny, J. Gordon, T. Heilweil, B. Stillwell, J. Guerrieri, E. Grossman, and S.-Z. A. Lo, "A small-sample, bi-directional scattering measurement system from 200-500 GHz," in *Proc. Antenna Meas. Techn. Association Conf.*, 2012, pp. 1-6.
[22] The MathWorks, Inc. Document: 1-D Interpolation. [Online]. Available: http://www.mathworks.com/help/matlab/1-d-interpolation.html.
[23] B. N. Taylor and C. E. Kuyatt, "Guidelines for evaluating and expressing the uncertainty of NIST measurement results," in *Nat. Inst. Stand. Technol. Tech. Note 1297*, Gaithersburg, MD, Sep. 1994.
[24] BIPM, IEC, IFCC, ILAC, ISO, IUPAC, IUPAP, and OIML, "Evaluation of measurement data—guide to the expression of uncertainty in measurement," *in JCGM 100:2008*, 1st Ed. Sèvres, France, Sep. 2008.

Sung Kim (S'08–M'09) received the B.E. degree in electronic engineering from the University of Electro-Communications, Tokyo, Japan, in 1996, the M.S. degree in electrical engineering from California State University, Northridge, CA, USA, in 2001, and the Ph.D. degree in electrical engineering from the University of Colorado, Boulder, CO, USA, in 2009.

Prior to joining the National Institute of Standards and Technology (NIST) in Boulder, CO, he was with Yokowo Co. Ltd. in Tokyo, designing planar antennas and LNAs for GPS and VICS systems, and millimeter-wave oscillators, and mixers integrated as Doppler modules for collision avoidance systems in vehicles. He also worked for Opnext Japan, Inc. (formerly Hitachi Ltd., and currently Oclaro, Inc.) in Yokohama, Japan, where he developed directly/externally-modulated 10/40-Gb/s optical transmitters for optical fiber communications, and further was with Soko Electronics Co. Ltd. in Osaka, Japan, developing electronics and embedded software for sensors for industrial and agricultural applications.

Since 2009, he has been with NIST as a Research Associate. His research interests include analytical and numerical modeling in electromagnetics, and developments and characterizations of RF and optical components.

David Novotny received the B.S. and M.S. degrees in electrical engineering from the University of Colorado, Boulder, CO, USA, in 1991 and 1996, respectively.

Since 1989, he has been working with the Electromagnetics Division, National Institute of Standards and Technology, Gaithersburg, MD, USA. From 1988 to 1999, he worked primarily on electromagnetic compatibility (EMC) issues: broadband/optical antennas, time-domain (real and synthetic) analysis of EMC facilities and RF materials, EM disruption of equipment and shielding of buildings, airframes, and other equipment. His research interests include electromagnetic studies of antennas, propagation, high-performance calibrations, EM measurements of active devices, and intentional and incidental interference effects and methods to enhance and mitigate them.

Joshua A. Gordon (M'14) received the Doctorate degree in optics and electromagnetics from the College of Optical Sciences, University of Arizona, Tucson, AZ, USA, in 2008.

He is a Physicist with the Electromagnetics Division, National Institute of Standards and Technology (NIST), Boulder, CO, USA. His research interests include new technologies for electric-field measurements such as robotic-based antenna metrology systems, optical techniques for antenna alignment, and atom-based electric-field and power sensing.

Jeffrey R. Guerrieri (M'14) has worked with the Electromagnetics Division, National Institute of Standards and Technology (NIST), Gaithersburg, MD, USA, since 1986.

He received the Department of Commerce Bronze Medal in 2009 for creating the World's first extrapolation range for measuring the on-axis gain and polarization of antennas for frequencies from 50 to 110 GHz. He also received the Department of Commerce Gold Medal in 2007 for creating and implementing the rigorous testing protocols and benchmarks needed to ensure the security and integrity of the new U.S. ePassport, and the Department of Commerce Bronze Medal in 2009 for the analysis and certification of the U.S. Passport Card architecture resulting in a mitigation of security threats and privacy concerns.